Cellulose (2024) 31:8149–8168
https://doi.org/10.1007/s10570-024-06105-2

ORIGINAL RESEARCH

Dielectric and thermal conductive properties of differently structured $Ti_3C_2T_x$ MXene-integrated nanofibrillated cellulose films

Subramanian Lakshmanan · Vida Jurečič · Vid Bobnar · Vanja Kokol

Received: 5 March 2024 / Accepted: 29 July 2024 / Published online: 2 August 2024

Abstract The fabrication of nanocellulose-based substrates with high dielectric permittivity and anisotropic thermal conductivity to replace synthetic thermoplastics in flexible organic electronics remains a big challenge. Herein, films were prepared from native (CNF) and carboxylated (TCNF) cellulose nanofibrils, with and without the addition of thermally conductive multi-layered $Ti_3C_2T_x$ MXene, to examine the impact of polar (−OH, −COOH) surface groups on the film morphological, moisturizing, dielectric, and thermal dissipation properties. The electrostatic repulsion and hydrogen bonding interaction between the hydrophilic surface/terminal groups on CNF/TCNF and MXene was shown to render their self-assembly distribution and organization into morphologically differently structured films, and, consequently, different properties. The pristine CNF film achieved high intrinsic dielectric permittivity (ε' ~ 9), which was further increased to almost ε' ~ 14 by increasing (50 wt%) the MXene content. The well-packed and aligned structure of thinner TCNF films enables the tuning of both the composite's dielectric permittivity (ε' ~ 6) and through-plane thermal conductivity (K ~ 2.9 W/mK), which increased strongly (ε' ~ 17) at higher MXene loading giving in-plane thermal conductivity of ~ 6.3 W/mK. The air-absorbed moisture ability of the films contributes to heat dissipation by releasing it. The dielectric losses remained below 0.1 in all the composite films, showing their potential for application in electronics.

Supplementary Information The online version contains supplementary material available at https://doi.org/10.1007/s10570-024-06105-2.

S. Lakshmanan · V. Kokol (✉)
Faculty of Mechanical Engineering, University of Maribor, Smetanova Ulica 17, 2000 Maribor, Slovenia
e-mail: vanja.kokol@um.si

V. Jurečič · V. Bobnar
Condensed Matter Physics Department, Jožef Stefan Institute, Jamova 39, 1000 Ljubljana, Slovenia

V. Jurečič · V. Bobnar
Jožef Stefan International Postgraduate School, Jamova 39, 1000 Ljubljana, Slovenia

Graphic abstract

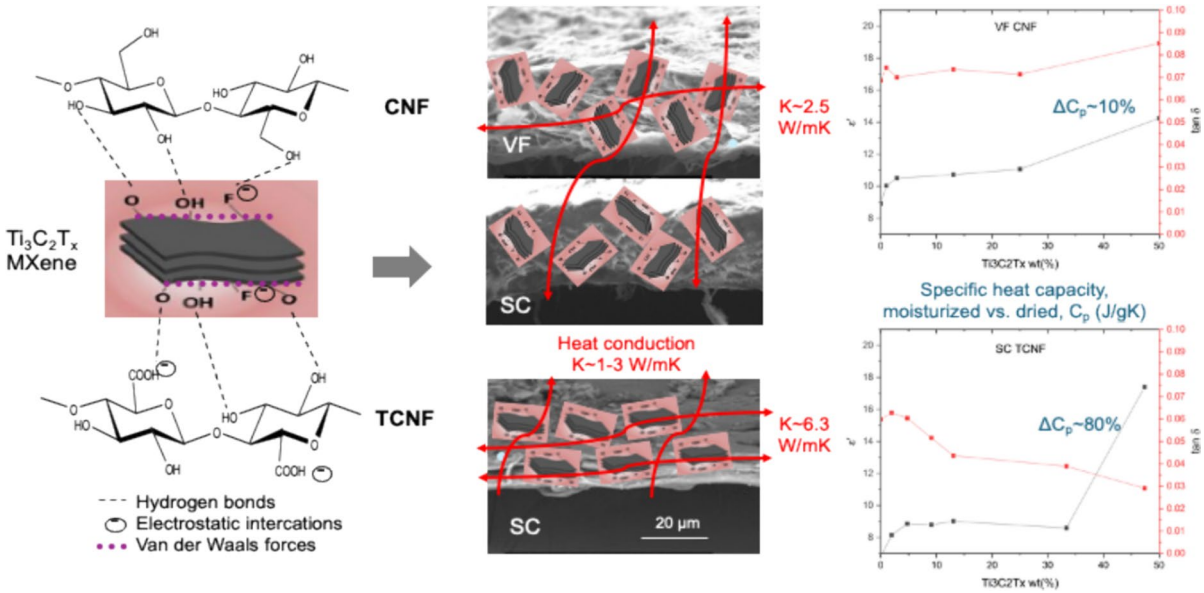

Keywords Nanofibrillated cellulose · $Ti_3C_2T_x$ Mxene · Film preparation · Moisture content · Thermal conductivity · Dielectric properties

Introduction

Nanocellulose, a structural polysaccharide with excellent electrical insulation properties and exceptional mechanical and thermal stability, has gained extensive attention recently in advanced organic electronics (Tao et al. 2020, 2021; Wang et al. 2021; Luo et al. 2023) to decrease the cost, and, above all, to replace toxic and non-biodegradable thermoplastic polymers (as, e.g., the most used biaxially oriented polypropylene / BOPP and polyvinylidene fluoride / PVDF in dielectric substrates), while retaining the devices' flexibility and lightweight, and boosting their recyclability. The existing synthetic dielectric substrates—used in, e.g., wearable electronics, medical/bioelectronics, solar cells, optoelectronics, and flexible displays—are also thermal insulators, while substrates of high anisotropic thermal conductivity and efficient dielectric properties are still not available. The research on nanocellulose-based substrates with such properties is also still very limited and in the initial phase.

The dielectric constant (ε') is a macroscopic manifestation of polarization, and the more polar the polymer is, generally the higher is the dielectric constant. Chemically, cellulose consists of linear chains of repeating D-glucopyranose units, connected covalently through β-(1 → 4)-glycosidic bonds, the symmetrical molecular structure of which, with dipole moments of C–OH bonds, can generate a strong polarity, and yield differently semi-crystalline structures by intra- and intermolecular hydrogen bonds between the hydroxyl (– OH) groups present on the cellulose backbone at the C6, C2, and C3 positions of the adjacent glucose units of the cellulose chains, all beneficial for the dielectric properties (Luo et al. 2023). The dielectric constant of native/pristine cellulose is, thus, related to a large number of polar – OH groups that can be dipole polarized by an alternating (AC) electrical current (Yun et al. 2009; Tao et al. 2020; Wang et al. 2023), ranging from 1.3 to 4.0 for CNF (resulting from its porous microstructure, and up to ~ 5.3 (measured at 1.1 GHz) for a densely packed nanocellulose paper (Inui et al. 2014), while having

a dielectric loss (tan δ) less than ~ 0.1 (Le Bras et al. 2015), which is, however, next only to the BOPP with a dielectric constant of ~ 2.2. The degree of polarization can additionally be manipulated by their engineering, such as modification of cellulose by replacing the – OH groups with more polar groups (e.g. carboxyl / – COOH, sulphate / – SO_3H, nitro / – NO_2, and nitrile / – CN; Luo et al. 2024), or introducing/grafting small chain segments (polyvinyl alcohol / PVA, polyaniline / PANI; Anju and Narayanankutty 2016) of large dipole moments onto it, and/or blending it with a relatively small content (near the percolation threshold, which is usually around 5wt%) of conductive (González et al. 2023) or high-k dielectric (Wang et al. 2021; Tao et al. 2021; Du et al. 2023; Zhao et al. 2023) nanofillers, thus increasing the permittivity while keeping a relatively low dielectric loss. However, by introducing a high-k inorganic ceramic nanofiller, such as $BaTiO_3$ (Tao et al. 2020) and TiO_2 (Tao et al. 2019), into the nanocellulose matrix is disadvantageous, because large amounts of ceramic fillers are necessary, causing brittleness of the nanocomposite and its breakage. Various types of two-dimensional (2D) conductive nanomaterials, such as carbon nanotubes (CNTs, Zeng et al. 2016; Tao and Cao 2020), graphene oxides (GO; Pottathara et al. 2016, 2018, 2021), and silver nanowires (AgNWs; Inui et al. 2014; Ji et al. 2017) with high aspect ratios have thus been studied recently (Table S1), resulting in dielectric permittivities between 10–3750 at low frequency (1 kHz). However, besides the cellulose's intrinsic properties (above all the included polar groups, crystal-amorphous ratio and hydrogen bonding), the presence of potential impurities (such as hemicellulose and lignin), chains` orientation, and, above all, moisture/water absorption ability, are other obstacles hindering its application as a dielectric material (Luo et al. 2023). Hygroscopicity is related to the density, including polar surface groups, intermolecular hydrogen bonding, and the density and moisture/water absorption ability of nanocellulose (Wang et al. 2023; Luo et al. 2023). Anyhow, the data of those physical properties on the dielectric of nanocellulose-based composites are still lacking.

In order to ensure good performance of an electronic device, a dielectric substrate with attached electronics should also possess good thermal transport capability to dissipate the heat produced by the Joule (resistivity) effect during its operation, thus not affecting their function adversely. The thermal conductivity of CNF-based films was found to be around 0.65–2.5 W/mK in the in-plane direction (Uetani and Hatori 2017; Xu et al. 2022, Table S2), which is 3–10 times higher than that of versatile plastics. This gives the potential for the development of cellulose-based materials with both dielectric and thermally conductive (or even heat dissipation) properties. The thermal diffusivity of CNF films can be improved further by reducing the thermal resistance at the interface between the fibrils. This can be obtained with an increased interaction (chemical and/or hydrogen bonding) between the cellulose fibrils through their highly aligned anisotropic (layer-by-layer) structure (~ 14 W/mK in-plane; Wang et al. 2022a, b), the introduction of multivalent ions (e.g. Ca^{2+}; Uetani et al. 2022) or thermally-conductive 2D nanofillers, such as graphene (164 W/mK in-plane and 5.0 through-plane; Chen et al. 2018a, b, c; Li et al. 2020) and boron nitride (12.68–21.39 W/mK in-plane; Xu et al. 2022, Zeng et al. 2017; Yang and Kim 2022) through specific structure construction, also resulting in an improved mechanical strength, electrical insulation, and flame retardancy.

Titanium carbide ($Ti_3C_2T_x$) type MXenes, recently developed 2D monolayer $Ti_3C_2T_x$ sheets of nanoscale thicknesses (10–20 nm) (Mathis et al. 2021), have also been shown as highly suitable for such applications, due to their high in-plane thermal (~ 10 W/mK) conductivity (Chen et al. 2018a, b, c), assigned to their well packed and aligned multi-layered structure enabling high phonon transport. Since it is affected by the amount of functional groups on the surfaces of the sheets, the lateral dimension between them and inter-sheet thermal resistance, the in-plane thermal conductivity of MXene film can be increased further (~ 55.8 W/mK) by improving the interaction between the nano-sheets using less delaminated MXene (Liu and Li 2018). Many MXene/polymer composites have been studied, and their thermal conductivity properties have been reported (Chen et al. 2021; Jin et al. 2020; Gao et al. 2021). It is believed that MXene forms chemical and/or hydrogen bonds with the polymer, which act as a bridge in the composites,

consequently forming a heat conduction network that promotes heat transfer between the polymer chains, while also preventing MXene oxidation (Habib et al. 2019). Meanwhile, MXene reduced the randomness of the polymer chain arrangement, and, thus, weakened the thermal vibrations (boundary conductance) and reduced the scattering of phonons (Kang et al. 2019) or phonon–phonon interactions in the interphase of the 2D nanosheets, which are essential for high thermal conductivity. The in-plane thermal conductivity of epoxy composite containing 1 wt% of few-layered Ti_3C_2Tx MXene is thus increased by ~ 141.3% (to ~ 0.58 W/mK) compared with that of neat epoxy at room temperature (Kang et al. 2019). The 27 µm thick PVA/MXene film containing 19.5 wt% of single/few-layered MXene nanosheets exhibited in-plane thermal conductivity of ~ 4.57 W/mK, while resulting in ~ 47.3 W/mK for a 3 mm thick PVA/MXene film containing 50 wt% of multi-layered MXene (Jin et al. 2020). The $Ti_3C_2T_x$ MXene was also shown to increase the dielectric properties of polymeric composites (such as an acrylic resin (Yang et al. 2023), polypyrrole (Shao et al. 2019), PVDF with $BaTiO_3$ (Feng et al. 2019), silicone rubber without (Zeng et al. 2022) and with Ag (Zeng et al. 2023), PVDF with MoS_2 (Wang et al. 2022a, b), given a dielectric constant of 6–143 and a dielectric loss of 0.001–0.23 at 1–0.1 kHz. Its addition (20 wt%) to nanocomposite films prepared from microcrystalline cellulose (MCC) through an LiCl/DMAc solvent was also shown recently to enhance (770%) film dielectric permittivity greatly (~ 71.4 at 0.1 kHz) at a very low increase of dielectric loss (from 0.39 to 0.70), owing to its interfacial polarization, while exhibiting in-plane thermal conductivity of ~ 8.52 W/mK related to the uniform dispersion and self-alignment of the MXene layered structure (Yan et al. 2023). In addition, recently published results on CNF/$Ti_3C_2T_x$ MXene-based composite film, containing 50 wt% of a few-layered $Ti_3C_2T_x$, showed a dramatic increase in in-plane thermal conductivity (from ~ 11.57 to ~ 21.2 W/mK) with increasing the temperature from 20 to 130 °C (Song et al. 2020). Such a linear relationship of thermal conductivity with increasing temperature was defined by the good water adsorption/desorption ability of MXene in a humid environment (Yu et al. 2022), and thus the possibility of making films with a passive thermal management effect based on moisture sorption–desorption principle (Wang et al. 2020). However, still rare studies have been performed for CNF-based composite films containing $Ti_3C_2T_x$ MXenes (Table S2), and no study yet on how they are affected by different polar groups on the CNF surface and their moisture adsorption/desorption ability.

In this work, the complete dielectric properties (dielectric permittivity, dielectric loss, and AC conductivity) of pristine (CNF) and TEMPO-oxidized CNF (TCNF) films prepared from an aqueous solution by different manufacturing methods (solution casting / SC and scalable vacuum filtration / VF; Du et al. 2023), were thus studied over broad frequency (1 Hz–1 MHz) and temperature (273–375 K) ranges. Various weight percentages of multi-layered $Ti_3C_2T_x$ MXene were included in the next stage, to verify the impact of CNF type (native vs. TEMPO-oxidized) on their self-assembly and interphase arrangement in composite films, and, consequently, on the dielectric and thermal (through-plane and in-plane) conductive properties. In addition, the ability of the as-prepared films to absorb moisture from the air was evaluated, to verify their complementary effect on the heat dissipation capacity (Wang et al. 2020).

Experimental

Materials

Cellulose nanofibrils (CNFs) and (2, 2, 6, 6-tetramethyl-1-piperidinyloxy) TEMPO-oxidized CNFs (TCNF) with chain-like structures, diameters of the 20–100 nm and 20–50 nm range, respectively, and lengths of a few (1–3)µm (Fig. S1), were prepared from bleached softwood pulp at the University of Maine (USA), The Process Development Center. The surface charges of around − 32.6 mV and − 35.1 mV were determined by dynamic light scattering analysis using a Zetasizer (Nano ZS ZEN360, Malvern Instruments Ltd., UK), being related to the presence of rare (~ 0.12 m mol/g) and numerous (~ 1.5 m mol/g) carboxylic groups, as evaluated by potentiometric titration (Mettler Toledo T-70 equipped with a combined glass electrode Mettler TDG 117, Metter Toledo d.o.o., Slovenia), respectively. The multi-layered

Table 1 The experimental design for composite films preparation, depending on the type of cellulose nanofibrils used (CNF, TCNF), the content of MXene ($Ti_3C_2T_x$), and the preparation method (vacuum filtration/VF followed by cold pressing, and solvent casting/SC)

Preparation method	Type of CNF (content of −COOH)	Concent. of MXene ($Ti_3C_2T_x$) (wt%)	Type and designation
VF + SC	CNF(~ 0.12 m mol/g)	0	CNF
		2–50	CNM-2, CNM-50
SC	TCNF (~ 1.5 m mol/g)	0	
		2–47	TCNM-2,… TCNM-47

2D titanium carbide ($Ti_3C_2T_x$) MXene powder with well-packed and aligned 10–20 nm thin nano-sheets of 10–20 µm large accordion-like morphology (Fig. S2) were purchased from Nanochemazone (Canada), and used as received. The dimethyl sulfoxide (DMSO) was purchased from Sigma-Aldrich GmbH (Germany).

Preparation of pristine and composite films

An overview of the experimental design for the preparation of nanocomposite films is collected in Table 1. The films were prepared by different methods, depending on the type of CNF used. While the CNF-based pristine and composite films were prepared by both (an upscalable, but low pressure) vacuum filtration (VF) and solution casting (SC) techniques, the TCNF-based films were prepared only by SC, due to the too-high water retention ability of TCNF to be vacuum filtered using the existing vacuum pressure. For the preparation of the films, the initial 0.69 wt% CNF and 1.1 wt% TCNF suspended in milli-Q water were used for the fabrication of pristine films (with final 0.1 g of CNF/TCNF weight mass), or film composites containing $Ti_3C_2T_x$ MXene. At the same time, various quantities of $Ti_3C_2T_x$ (0.002, 0.005, 0.015/0.017, 0.0345/0.040, 0.057, 0.1035, 0.3105, 0.9315 g) were dispersed homogeneously in 15 mL DMSO by ultrasonic processor (VCX 750, Sonics & Materials, Inc., USA), for 1 h at 20% amplitude. Finally, each of the DMSO-dispersed $Ti_3C_2T_x$ was mixed with the water-suspended CNF/TCNF, and stirred again for 1 h to get homogeneous CNF/TCNF-$Ti_3C_2T_x$ dispersions with a final 2 wt%, 5 wt%, 9 wt%, 13 wt%, 25 wt%, 33 wt%, 50/47 wt%, and/or 75 wt% of $Ti_3C_2T_x$. The as-prepared CNF/$Ti_3C_2T_x$ dispersions were vacuum filtered (VF) through a cellulose filter with a pore size of 5–8 µm (Rotilabo 13A, Carl Roth GmBh & Co. KG, Germany), transferred in a wet stage to polystyrene Petri dishes of 6 cm in diameter (Greiner Bio-one GmbH, Austria), left to dry at room temperature, and additionally pressed for 5 h at 4 bar in a Perkin Elmer laboratory hydraulic press (Scientific Instruments, USA). In the case of the solvent casted (SC) films, the dispersions were poured directly into the Petri dishes, and dried at room temperature. The composite films were designed as, e.g., CNM-2 or TCNM-2, where M stands for $Ti_3C_2T_x$ MXene and CN for CNF, or TCN for TCNF, and the number refers to the wt% of $Ti_3C_2T_x$ in the film. The pristine CNF/TCNF films were prepared in the same way. The films were stored in a desiccator (DIN 12491) to minimize their hygroscopicity before further usage.

Characterizations

Thickness and density

The thickness of the films was measured using a dial thickness gauge, F1000/30 (Käfer Messuhrenfabrik GmbH & Co. KG, Germany). The volumetric density (g/cm^3) was calculated from the weight mass, diameter and thickness of the samples. The presented results are the arithmetic mean values and the Standard Deviations of at least two independent measurements, obtained on pre-conditioned samples at 23 ± 1 °C and 65 ± 2% RH for 24 h.

Moisture content

The samples were cut into squares of 1 × 1 cm, conditioned at 23 ± 1 °C and 65 ± 2% RH for 24 h, and dried in a moisture analyzer (DBS 60–3, Kern & Sohn GmbH, Germany; standard drying with automatic switch off) to the absolute dry weight. The moisture (M) content (g/g of the film, expressed in %) was calculated as $(M_w\text{-}M_d)/M_d \times 100$, where M_w is wet/moisturized (conditioned) and M_d the absolutely dried mass (pre/dried at 100 °C for about 1 h), and the time (t, min) of drying was recorded. The moisture evaluation experiments were performed for two independent measurements for each selected sample, and the data presented as the arithmetic mean values with standard deviations.

Scanning *electron* microscopy (SEM) and energy dispersive X-ray (EDX) spectroscopy

SEM imaging was performed by using a low-vacuum scanning electron microscope, FEI Quanta 200 3D (Thermo Fisher Scientific Inc, USA), equipped with an EDX spectrometer (Inca 350, Oxford Instruments Nanoanalysis, UK) for micro-chemical mapping. The sample surfaces and cross-sections were analyzed.

X-ray photo-*electron* spectroscopy (XPS)

The XPS measurements were performed with a Supra plus device (Kratos, Manchester, UK), equipped with an Al Kα excitation source. During the spectra acquisition, the charge neutralizer was on. The binding energy scale was corrected using the C–C/C–H peak at 284.8 eV in the C 1 s spectra. The samples were attached to the sample holder using carbon tape. The measurements were carried out at a 90° take-off angle at a pass energy of 20.0 eV and a step of 0.1 eV. The spectra were recorded for at least two locations on each sample, and processed using the ESCApe 1.5 software (Kratos).

Fourier transform infrared (FTIR) spectroscopy

The Fourier transform infrared spectra were recorded by using a Spectrum One spectrometer (Perkin-Elmer Inc., USA). The transmission measurements were carried out in the range of 400–4000 cm^{-1}, with 16 scans and a resolution of 4 cm^{-1}. The Spectrum 5.0.2 software program (version 10.6.1.) was applied for the data analysis. A few measurements were made of pre-conditioned samples at 23 ± 1 °C and 65 ± 2% RH for 24 h per film.

Dielectric spectroscopy

For the dielectric measurements, the surfaces of the films were covered by ~ 100 nm thick sputtered gold electrodes having a diameter of around 4 mm. The complex linear dielectric constant $\varepsilon^*(\omega,T) = \varepsilon' - i\varepsilon''$ was measured by an Alpha high-resolution dielectric analyzer (Novocontrol Technologies GmbH, Hundsangen, Germany). The amplitude of the probing AC electric signal was 1 V. The values of the real part of the dielectric constant, i.e., the dielectric permittivity ε', and the values of the real part of the electrical conductivity, σ', were calculated from the actual measured quantities, the capacitance C and electrical conductivity G via $\varepsilon' = (Cd)/(\varepsilon_0 S)$ and $\sigma' = Gd/S$, where d is the sample thickness, S is the electrode area, and $\varepsilon_0 = 8.85 \times 10^{-12}$ As/Vm is the permittivity of the free space. The imaginary part of the dielectric constant ε'' is connected to the electrical conductivity via $\sigma' = 2\pi\nu\varepsilon_0\varepsilon''$. The dielectric response was detected either as a function of frequency at room temperature, or at several frequencies during the heating and/or cooling runs, with the rate of ± 0.75 K/min. The temperature of the samples was stabilized within ± 0.01 K by using the lock-in bridge technique with a platinum resistor Pt100 as a thermometer. One measurement was performed per film.

Thermal diffusivity and conductivity

The thermal diffusivity in the through-plane configuration was measured for the selected film samples by the laser flash method using an LFA 467 HyperFlash (Netzsch Holding, Germany) at the temperatures of 20 °C (19.9 °C), 40 °C, 60 °C, 80 °C and 100 °C; the in-plane configuration measurement could be performed only for samples containing a higher content of $Ti_3C_2T_x$ due to the samples unevenness. Five laser pulses (xenon of 10 J/pulse) for 20 µs were performed at each temperature. The samples were spray coated with graphene before the

analysis and pre-conditioned at 23 ± 1 °C and 65 ± 2% RH for 24 h. The thermal conductivity K (W/mK) was calculated as $K = \alpha \times \rho \times Cp$, where α and ρ are the thermal diffusivity (mm^2/s) and density (g/cm^3) of the film, respectively, and Cp is the specific heat capacity (J/gK) measured with the classic sapphire method according to the standard procedure (User Com 7, Mettler Toledo GmbH, Schwerzenbach, Switzerland, 1998) using a differential scanning calorimeter Mettler Toledo DSC1 (Switzerland). The samples in the form of thin layers were carefully cut with a special tool to obtain the circles suitable for placement in 20 µ L DSC crucibles. The initial masses of pre-conditioned (moisturized) samples of about 4–8.5 mg were obtained by placing several (4–6 layers) layers on top of each other and pressing them firmly together with a Teflon rod. The same Teflon rod was used to press a lid onto the samples to ensure good thermal contact and to prevent the composite material from bending during heating. Weighing was performed on a Metter Toledo micro balance MX5 with an accuracy of 1 µg. In the first measurement, two empty crucibles with the pressed lid (blank curve) was measured. In the second measurement, a sapphire disc with a known temperature dependence in C_p was measured on a sample side. The temperature program for these two measurements was identical to that for the sample measurements. For the C_p determination of the moisturized samples, the sample crucibles were covered with the lid, which was not pierced, and put into a DSC cell, which was cooled from room temperature to 0°, left at 0 °C for 15 min to reach thermal equilibrium, and then heated to 110 °C at a rate of 10 K/min. In addition, samples were covered with a pierced lid and the cell with the inserted sample was first heated to 110 °C at a dry air flow of 50 mL/min (so that the adsorbed moisture was evaporated), then cooled to 0 °C, and thermostated at this temperature for 15 min before the dynamic measurement was performed again at a rate of 10 K/min up to 110 °C; thus the C_p of the pre-dried sample was determined. The C_p difference (expressed in %) was calculated as $100—(Cp_w/Cp_d) \times 100$, where Cp_w is the value obtained by the first measurement method (i.e. for the moisturized sample) and Cp_d by the second method (i.e. for the pre-dried sample). Three measurements were made per each selected film, and the results were given as an average value with a Standard Deviation.

Results and discussion

Morphological, structural and physico-chemical properties

The morphology (surface, cross-section) of differently prepared films and interactions between the $Ti_3C_2T_x$ MXene and CNF/TCNFs were studied by SEM imaging, EDX, XPS and FTIR spectroscopy.

As shown in the SEM image, presented in Fig. S2a, the $Ti_3C_2T_x$ MXene has a typical accordion-like morphology (ranging from a few up to 20 µm), consisting of a few nm thick nanosheets, stacked together in a multi-layered structure. The lamellas openings of the MXene sheets are also very visible, which is due to their exfoliation (Alhabeb et al. 2017; Syamsai et al. 2017). The elemental analysis obtained by EDX elementary analysis confirmed the composition of Ti, C, and O, as well as the presence of F. The XPS analysis (Fig. S2b) also confirmed the presence of terminated (T_x) O and F functional groups (such as −OH, −O, and −F) on the outer surfaces of the MXene layers by the peaks of O 1 s at ~ 532 eV and F 1 s at ~ 685 eV, respectively (Zhang et al. 2017). The Ti 2p spectra represent Ti–C components, whose binding energy position depends on the local bonding of the terminal fluorine (F) and oxygen (O) species. The presence of C can be related to the presence of impurities such as hydrocarbons (CH-x), alcohol (C–OH), and carboxyl (−COOH) components (Näslund et al. 2020). From a relatively high percentage of O-components, some of them were also expected to be in the form of TiO_2, because the samples were exposed to the laboratory atmosphere and vigorous mixing/filtration during preparation.

Figure 1a (as well as Fig. S3a) show SEM images of the VF CNF-based films prepared with and without different contents of $Ti_3C_2T_x$ MXene. The smoother surface, but randomly interwoven arranged cellulose fibrils, both on the surface and in the cross-section, are visible in the case of the pristine (~ 38 µm thick) CNF film. By the addition of a smaller quantity (5–10wt%) of $Ti_3C_2T_x$ the fibrils become more longitudinally oriented and the film more densely structured with integrated and CNF-coated $Ti_3C_2T_x$ micro-large MXenes; a similar effect was observed for the film (containing 5 wt% $Ti_3C_2T_x$) prepared by the SC method (Fig. S3b). This structure is collapsed for the film prepared with higher (50wt%) $Ti_3C_2T_x$ content,

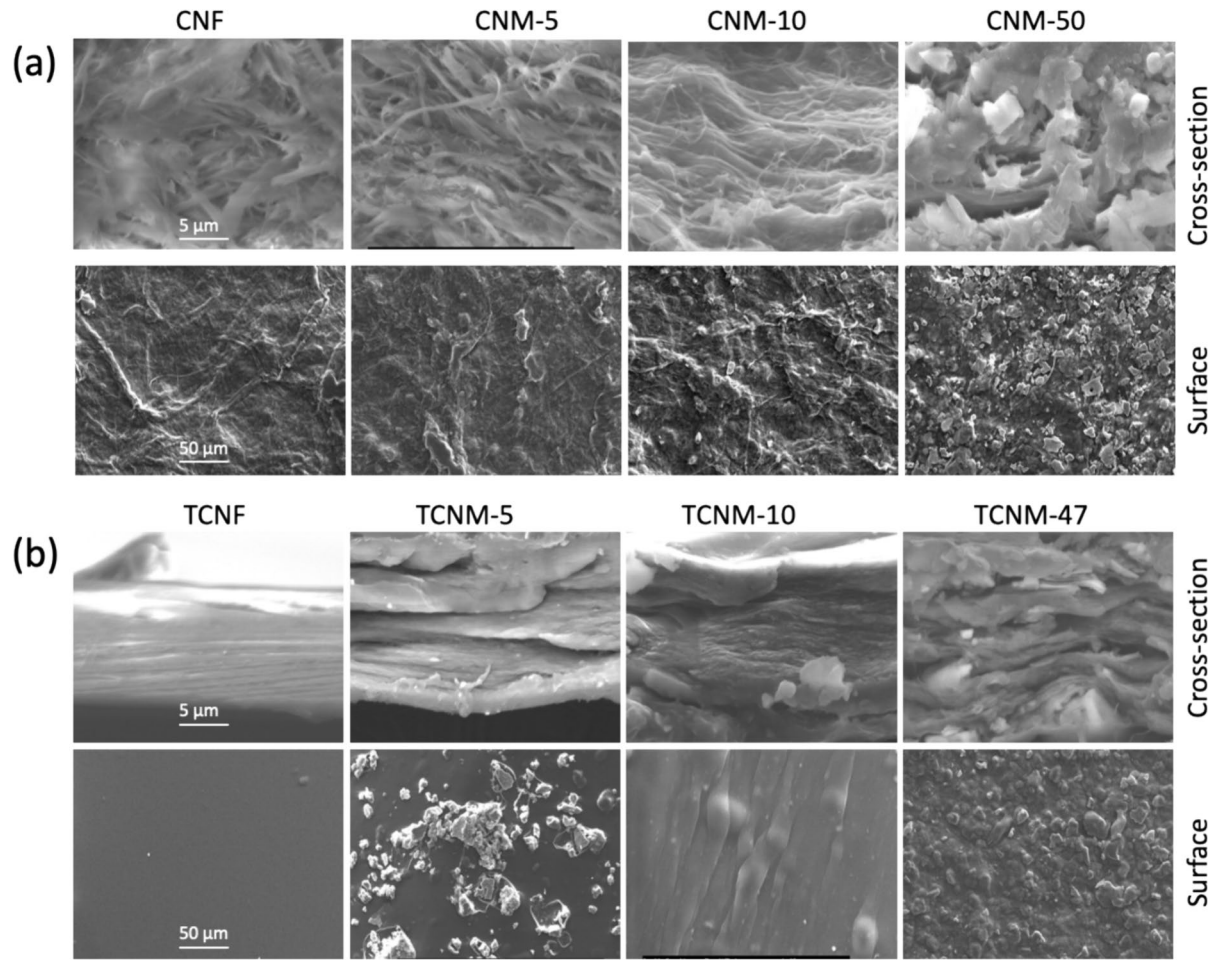

Fig. 1 Cross-sections and surfaces of the representative **a** VF CNF/CNM and **b** SC TCNF/TCNM films containing different contents of $Ti_3C_2T_x$ (5, 10 and 50/47wt%)

leading to a more open/porous structure in the bulk, and predominantly deposited, differently oriented and aggregated $Ti_3C_2T_x$ MXenes on the surfaces. On the other hand, the pristine TCNF film prepared with the SC method (Figs. 1b and S3b) was fully transparent, the thinnest (~ 19 µm) and highly compact with parallelly aligned fibrils and a smooth surface. Such a well-oriented (and still relatively compact, ~ 25 µm thick) structure was preserved for the TCNM composite films containing up to 10 wt% $Ti_3C_2T_x$. A more open and thicker (~ 88 µm) structure is built with less uniformly distributed $Ti_3C_2T_x$ MXenes at higher (47wt%) concentration, which, however, were still fully integrated in the film and covered by the fibrils. The surface topography and roughness of such composite films did not increase drastically, although the MXene size ranged from a few up to ~ 20 µm in lateral diameters (Fig. S2a). Such a structure could be attributed to better dispersibility, and, consequently, a more homogeneous distribution of $Ti_3C_2T_x$ MXene in the TCNFs network. The TCNF possesses a large amount of anionic carboxylate groups ($-COO^-$) on the cellulose C6 hydroxyls ($-OH$), which creates electrostatic repulsion between the fibrils and facilitates their individualization in an aqueous solution (Fig. S1), resulting in weakening the hydrogen bonding, and, subsequently, generating a stable and uniform dispersion. The presence of $Ti_3C_2T_x$ with negatively functional surface groups ($-OH, -O,$ and $-F$; Fig. S2) additionally affects their distribution and orientation. This also depends on the MXene content, as well as the quantity and localization of the surface groups

on both components. The composite films with more randomly oriented CNFs and distributed aggregates of MXene are thus formed by using CNFs, where the effects of the different preparation protocols (VF and SC) were found negligible, and the interactions between the CNF matrix and MXene were influenced mainly by the surface groups of $Ti_3C_2T_x$. On the contrary, the TCNM composite films clearly present a more compact and hierarchically aligned (a nacre-like layered) structure with negligible agglomeration (attributed to their better dispersibility) and orientation of both components in the planar direction, in good agreement with previous works (Jin et al. 2022; Liu et al. 2022); it also appears that some MXenes were exfoliated during drying and appeared on the film`s outer surface. In all cases, CNF/TCNF, acting as interlayer spacers between the MXene sheets, influenced their connecting and the structure of the films. The elemental mapping of representative films, performed by EDX analysis (Fig. S4), also supported these results by a differently homogeneous distribution of C, Ti, O, and F atoms across the cross-section of the composites, their dispersibility and compatibility. According to these analyses, the C:Ti and O:Ti ratios of CNF/$Ti_3C_2T_x$ (CNM-10) are also higher (58:2 and 38:2, respectively) than those of TCNF/$Ti_3C_2T_x$ (TCNM-10; 58:1 and 39:1, respectively), which indicates that the Ti terminal groups of $Ti_3C_2T_x$ were interacting differently (i.e. intra/inter-molecular hydrogen bonding and van der Waals forces) with the surface groups of the CNF (in the TCNM film case) than TCNF (TCNM), due to the presence of electrostatic repulsion between the hydrophilic surface groups in the latter.

FTIR spectra of the $Ti_3C_2T_x$ MXene powder, pristine CNF/TCNF and selected CNM/TCNM composite films were performed (Fig. 2), to analyze the characteristic functional groups and interfacial interactions between them. The spectra of $Ti_3C_2T_x$ MXene had small shoulders at about 3400 cm^{-1}, 1630 cm^{-1}, 1000 cm^{-1}, and more intensive at 600–500 cm^{-1}, corresponding to the stretching vibration of the –OH, C = O, C–F, and Ti–O bonds, respectively (Cao et al. 2018; Yan et al. 2023). The pristine CNF film shows characteristic transmittance bands for cellulose at about 3340 cm^{-1} (assigned to − OH stretching), 2920 cm^{-1} (CH_2 stretching), 1410–1420 cm^{-1} (CH_2 bending), 1360–1310 cm^{-1} and 1150–1110 cm^{-1} (CH stretching and bending), 1030 cm^{-1} (C–O–C stretching vibration of glucopyranose linkage, and − OH bending), 890 cm^{-1} (associated with cellulosic β-glycosidic linkages), and 660 cm^{-1} (− OH out of plane bending). The larger band at about 1600 cm^{-1} in the TCNF spectrum was attributed to the stretching vibrations of C = O, arising from the presence of carboxylic (− COOH) groups. All the characteristic peaks for CNF/TCNF and $Ti_3C_2T_x$ are found in both spectra of the composite films, but

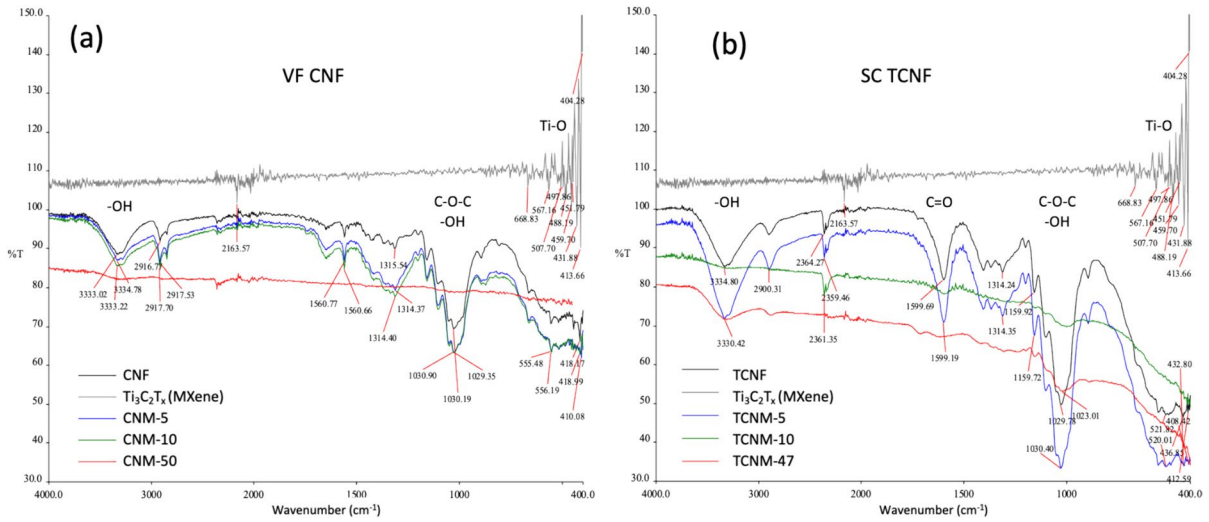

Fig. 2 FTIR spectra of representative **a** VF CNM, and **b** SC TCNM composite films, compared to the pristine CNF/TCNF films prepared with the same method and $Ti_3C_2T_x$ MXene powder

with different intensities, which indicated that the $Ti_3C_2T_x$ MXenes were associated differently with the cellulose fibrils. The bands assigned to the – OH and – COOH surface groups (above all those at about 3334 cm^{-1}, 1600 cm^{-1} and 1030 cm^{-1}) in the composite films were broadened, weakened, and, in the case of TCNM films, shifted slightly to a lower (at 3334 cm^{-1}) or higher (at 1030 cm^{-1}) wavelength with increasing of $Ti_3C_2T_x$ content films, all implying reducing hydrogen bonding between the – OH, – O and C = O atoms of the adjacent glucose groups in the CNF/TCNF, due to their formation with the surface groups of Ti_3C_2Tx (– OH, – O, and – F, Fig. S2). It can also be observed that, at higher (50/47wt%) Ti_3C_2Tx content, the presence of a small shoulder for the – OH groups (at 3334 cm^{-1} and 1030 cm^{-1}) and peaks for – COOH groups (at 1600 cm^{-1}) in the case of TCNM-50 composite were still present, indicating their availability. This is also in line with the structural evidence supported by EDX patterns (Fig. S4), as discussed above, and both results proved the structurally different integrity of Ti_3C_2Tx within the TCNF matrix and their intercalations. Spherically larger and negatively charged carboxylic (– COOH) groups on the TCNF backbone have more freedom of movement (Zhao et al. 2023) and also more space for their arrangement, thus forming a more uniformly packed composite with an increased contact area between them (Zhan et al. 2019), as already confirmed by the SEM images (Figs. 1 and S3), but with different interactions; beside the stronger hydrogen bonding and van der Waals forces, electrostatic

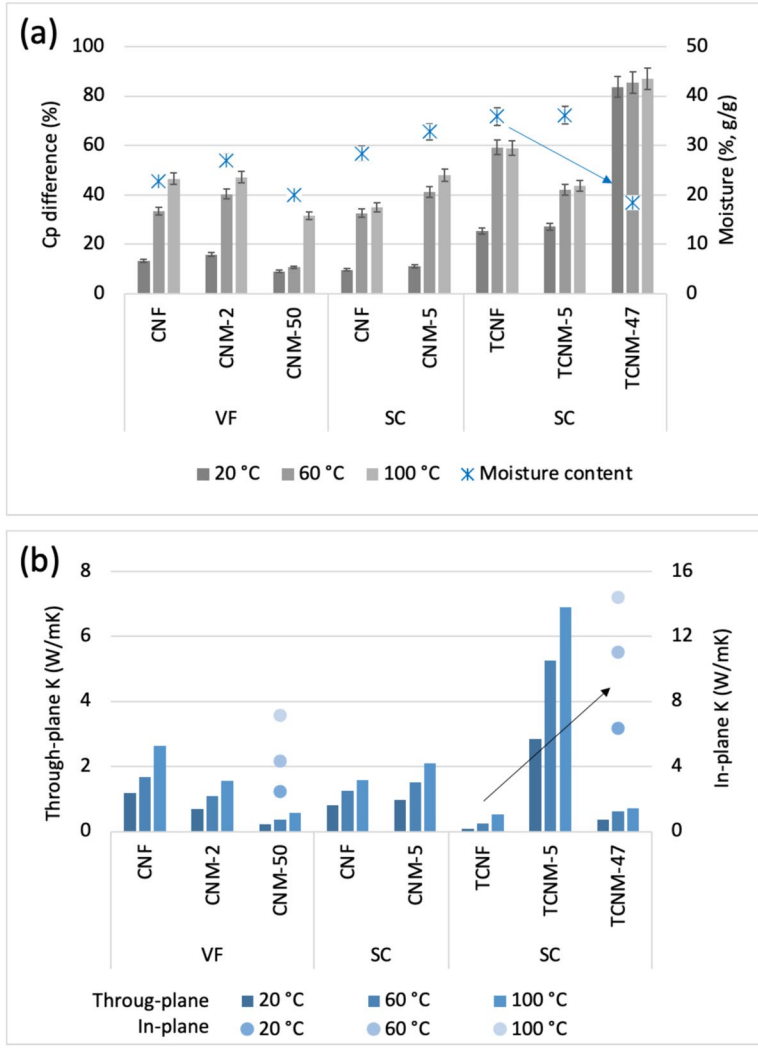

Fig. 3 **a** The difference (moisturized vs. pre-dried, expressed in %) in specific heat capacity (Cp) of selected VF CNF/CNM and SC CNF/CNM and TCNF/TCNM films related to their moisture content, and **b** their thermal conductivity (K) values (for moisturized samples), depending on the temperature

repulsion interactions were also present. On the other hand, the $Ti_3C_2T_x$ MXene was interacting with the CNF network via predominant hydrogen bonding, but given a more open morphological structure due to randomly distributed fibrils. It can also be observed that, with an increase of the MXene content, the characteristic peaks intensity for the TCNM film weakened faster (from about TCNM-10) than that for CNM (from about CNM-50), further suggesting differently strong interactions between the components (both between the fibrils themselves like those with MXenes) and their distribution through the films, directed highly by the fibrils self-assembly, depending on the composite`s morphological structure.

Finally, the physico-chemical properties (thickness and density) and moisture content in differently prepared films were determined, to evaluate their effect on specific heat capacity and thermal conductivity. As seen from the results presented in Fig. S5, the density of the films varied inversely proportionally with the thickness by increasing the content of $Ti_3C_2T_x$, which also had a significant effect on their moisture absorption capacity when exposed to 23 °C and 65% RH for 24 h. The moisture content for SC TCNF-based films was thus generally higher (by up to 14% if expressed in g/g, or even between 2000–3000% if expressed in g/cm^3) as compared to the other films prepared with or without up to 10 wt% addition of $Ti_3C_2T_x$, and it was also reduced more intensively (to around 20%, g/g or 543%, g/cm^3) with its further increase of $Ti_3C_2T_x$ to 47 wt% (VF CNM-50 given 18.5%, g/g or 26%, g/cm^3 reduction in moisture).

The films with a higher moisture content also had a higher difference (an increase, Fig. 3a) in specific heat capacity (Cp) when comparing the pre-dried and moisturized (i.e. pre-conditioned) samples (Fig. S6), confirming the different presence of moisture, as well as its removal/evaporation kinetic. In addition, a slight increase of Cp values for pre-dried samples by increasing the temperature (from 20 to 100 °C), also confirms the still accumulated small amount (estimated to be less than 3%, similar to the values obtained study by Uethani et al. 2022) of moisture within the films, which desorption by raising the temperature was comparable regardless of the used CNF or the method of film preparation, but generally lower for films containing MXene; only in the case of TCNM-50, the most densely prepared film, this effect was insignificant, i.e. in the range of SD (±5%). This indicated differently interfibrillar/intermediately adsorbed moisture, whose accumulation depends on the fibrils' morphological and hydrophilic (type and amounts of available surface groups) nature, interactions between them and with MXenes, and their distribution in the composite film. Therefore, there was an obvious difference in the Cp increase (moisturized vs. pre-dried, expressed in %, Fig. 3a) of the films prepared with higher (50/47wt%) $Ti_3C_2T_x$ addition and similar moisture content (20/18.5%, g/g); i.e. a slight reduction for the CNM-50 sample and an almost one-time increase for the TCNM-47 one, independent of the temperature, that also confirmed the effect of the films morphological structure (Fig. 1) on their water desorption ability. While freely absorbed water requires low energy to remove, the interphase trapped water molecules (Kulasinski 2017; Chen et al. 2018a, b, c) or bound (through hydrogen bonds or intermolecular interactions) to the available interphase surface groups on the cellulose fibrils (−OH/COOH) or MXene (−OH, −O, and −F; Yu et al. 2022) can be removed under specific drying conditions, to overcome capillary forces and other interactions.

The corresponding through-plane thermal conductivity (K) (Fig. 3b) of CNF-based films with a thicker and more open structure (associated with much more randomly oriented and distributed tightly CNF-coated MXene, Fig. 1a), thus reduced gradually with the addition of $Ti_3C_2T_x$ (from ~ 1.18 to ~ 0.21 W/mK) at 20 °C, while showing a slight increase (to ~ 2.63 and ~ 0.57 W/mK, respectively) by increasing the temperature, due to the slower release of the interphase-absorbed moisture, as is evident from the results presented in Fig. 4a. A much higher through-plane thermal conductivity (~ 2.85 W/mK) was achieved for the TCNF sample, with 5 wt% of $Ti_3C_2T_x$ loading (TCNM-5), which is higher than the recently published results on VF CNF based film containing 50 wt% of a few-layered $Ti_3C_2T_x$ (Song et al. 2020), showing also a percolation behavior. This was attributed to the reorientation/exfoliation of MXene (Figs. 1b and S3b) and enhanced composite surface roughness playing a major role in heat conduction (Zeng et al. 2017; Hu et al. 2021). Its further increase with increasing the temperature (to ~ 6.89 W/mK at 100 °C) also indicates a greater contribution of surface adsorbed (and capacitative higher, Fig. 4b) moisture, and its gradual release from such

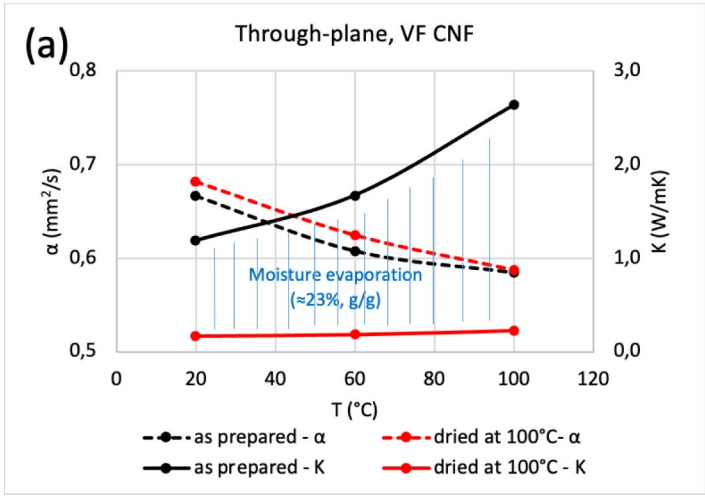

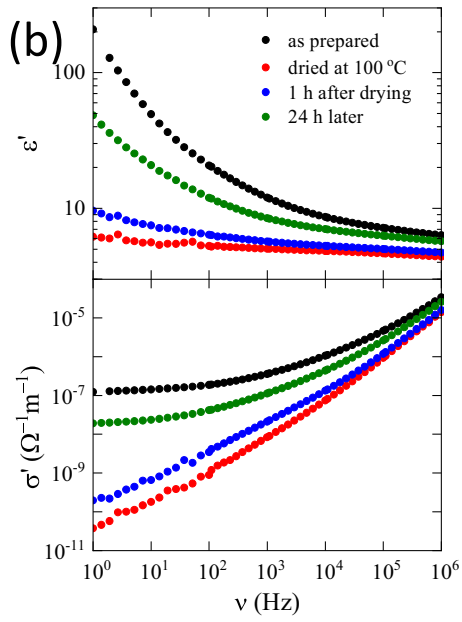

Fig. 4 **a** Temperature dependence of through-plane thermal diffusivity (α) and thermal conductivity (K), and **b** Frequency dependence of dielectric permittivity (ε') and AC electrical conductivity (σ') at room temperature for the (i) as prepared, and (ii) absolute dried (at 100 °C) VF CNF film, as well as (iii) 1 h and 24 h after drying

a structure, thus confirming its complementary contribution; to the – COOH groups bound water molecules also evaporating faster during the heating than those bound on the – OH ones, while also weakening the intra-chain hydrogen bonds between the fibrils and the integrated MXenes. Such results can also be supported by the fact that the thermal diffusivity (α) (Fig. S7) and Cp (Fig. S6) values of plain samples (without MXene addition) were strongly dependent on the moisture content (i.e. decreasing with increasing moisture due reduced phonon propagation), as already established by other studies (Izakura et al. 2021), but almost insignificant with increasing the temperature, which again confirms an important effect of the film's morphological structure and density. Furthermore, the in-plane thermal conductivity measurements, which could be evaluated only for samples with higher $Ti_3C_2T_x$ content (otherwise the values had too much scatter and a uniform trend to be able to determine the true values), resulted in ~ 2.48 W/mK for the CNM-50 and ~ 6.35 W/mK for the TCNM-47. Such a thermal conductivity of the TCNM samples containing a higher amount of MXene can thus be attributed to both the multi-layered structure of $Ti_3C_2T_x$ nanosheets that can easily construct heat-spreading pathways in the in-line direction, as well as the more homogeneous distribution of MXene between the TEMPO-oxidized CNFs, forming a densely packed and (in-plane) parallelly aligned structure (Fig. 1b), being thus also favorable for heat dissipation in the through-plane direction (Liu and Li 2018). TCNFs can also fill the gaps between adjacent nanosheets of $Ti_3C_2T_x$ easily, enhance the connection between them through different interactions (as confirmed by the FTIR spectroscopy, Fig. 2), therefore, decreasing the interfacial thermal resistance in both directions, and/or direct the heat transfer along the integrated $Ti_3C_2T_x$ nanosheets of multi-layered MXene (Chen et al. 2018a, b, c). Finally, the TCNM-47 film also needed a longer time to desorb the absorbed moisture (Fig. S5) which can contribute complementarily touyor the (through-plane) heat dissipation performance.

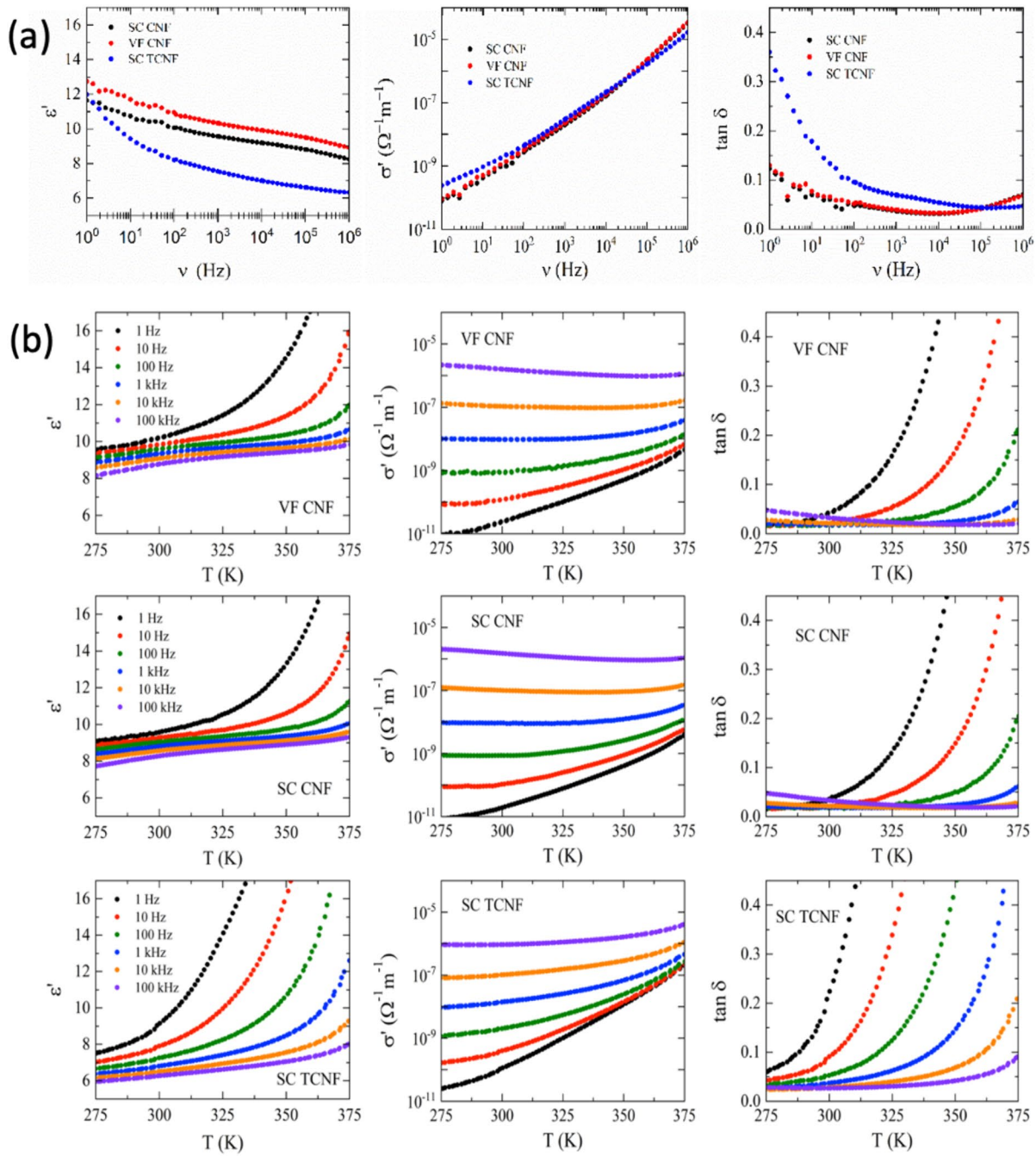

Fig. 5 **a** Frequency dependence of dielectric permittivity (ε'), AC electrical conductivity (σ'), and dielectric loss (tan δ), detected at room temperature, for differently prepared films. **b** Temperature dependent dielectric response of the films

Dielectric properties of pristine and composite CNF/TCNF films

It has been reported that the intrinsic dielectric permittivity (ε') of the pristine CNF film is almost independent of temperature (Jose et al. 2021). Other studies, including those of (Le Bras et al. 2015; Kovalov et al. 2017), revealed that the AC electrical

conductivity (σ') of CNF films increases strongly with the increase of frequency, and, moreover, that humidity plays a very important role; the electrical conductivity thus increases from 10^{-10} to 10^{-7} S/cm when the relative humidity increases from 10 to 80%. Our results, presented in Fig. 4b, for a representative CNF film prepared by the VF method, are in line with the previously published results. The absorbed moisture enhances the values of both ε' and σ' strongly at low frequencies in the pristine, i.e. as prepared film sample (note the logarithmic ε'-scale). After one hour of drying at 100 °C the sample values at low frequencies decreased by orders of magnitude. However, they increased again when the sample was exposed to the air atmosphere, due to the reabsorbed moisture. At a high (1 MHz) frequency this effect was almost negligible, which suggests that the data detected at this frequency reveal the intrinsic response of the samples.

To minimize the effect of moisture, all the films presented and discussed below were dried for one hour at 100 °C before the dielectric measurements. The frequency- and temperature-dependent dielectric responses of pristine CNF and TCNF films, prepared by different methods, were studied first (Fig. 5). In the natural state, the dipoles (−OH groups) in cellulose materials are oriented randomly and arranged freely. When the cellulose material is exposed to an external electric field, the dipoles orient in the direction of the field, which results in a non-zero electric polarization (Tao et al. 2020; Wang et al. 2023). However, the dielectric constant generally increases with a lowering of the frequency, either due to the free space charge, impurities contributions, or external effects, such as the presence of surface layers (for example, due to the formation of Schottky barriers) (Lunkenheimer et al. 2002; Pottathara et al. 2016, 2018). Indeed, as seen in Fig. 5a, the dielectric permittivity at room temperature increased slightly at lower frequencies. On the other hand, the AC electrical conductivity increased strongly with the increase of frequency in all samples. Consequently, the dielectric losses undergo a crossover from decreasing to increasing behavior. However, according to other studies, hydrogen bonding between the glucose units in cellulose chains formed during the drying at 100 °C should hinder the rotational movement of dipolar −OH groups in the case of CNF, thus giving lower dielectric permittivity. On the other hand, the presented −COOH polar groups with a higher degree of orientation polarization should increase it for the TCNF film (Luo et al. 2024), which was, however, not the case in our samples.

The intrinsic dielectric permittivity, evaluated at the highest (1 MHz) measurement frequency, for CNF films is almost independent of the temperature (Fig. 5b). On the other hand, the values obtained at low frequencies increased with increasing the temperature, due to the higher mobility of the free

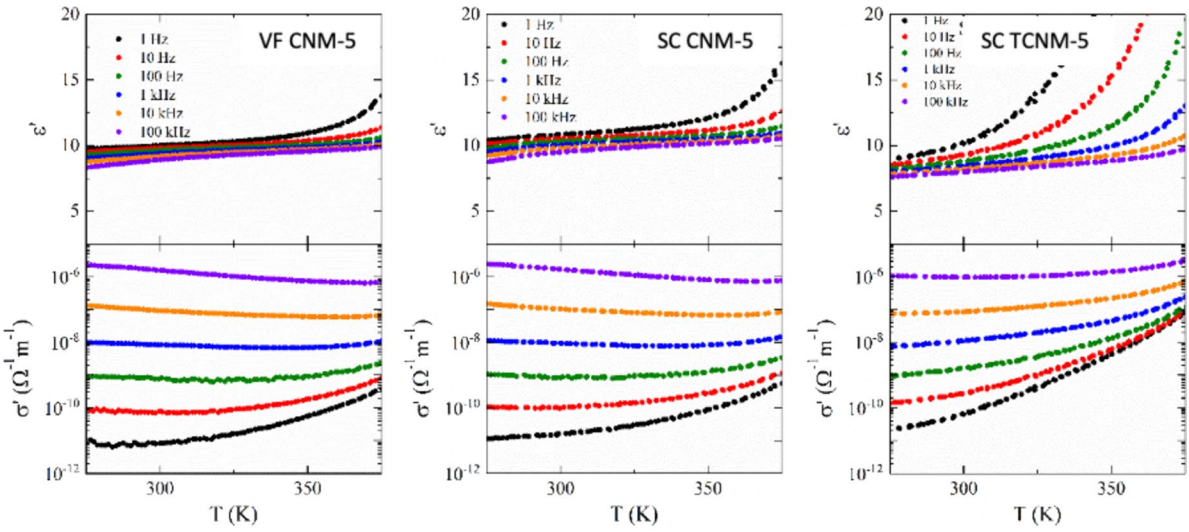

Fig. 6 Temperature dependence of dielectric permittivity (ε') and AC electrical conductivity (σ') of differently prepared (VF, SC) composite CNF/TCNF films with 5 wt% addition of $Ti_3C_2T_x$ MXene

space charges, and the same applies to dielectric losses. The cellulose fibril is a semi-crystalline layered structure of cellulose chains that trap space charges efficiently (Windmill et al. 2007), which also accumulate at the interface between them (Abdel-karim et al. 2018). The accumulated charges diminish the movement of cellulose dipoles via the pinning effect, which could be the origin of the slightly lower intrinsic dielectric permittivity of the TCNF sample. The number of free space charges is obviously higher in the TCNF film due to the presence of polar −COOH groups having more freedom of movement (as already confirmed by FTIR spectroscopy, Fig. 2b), where the increase at lower frequencies was more pronounced during both the frequency-dependent and temperature-dependent experiments. The difference in the dielectric response between the CNF and TCNF samples could also originate from the morphologically differently structured films (Figs. 1 and S3), i.e. fibrils' orientation, homogeneity and density in the film. However, the method (VF vs. SC) of CNF film preparation almost did not affect its dielectric properties.

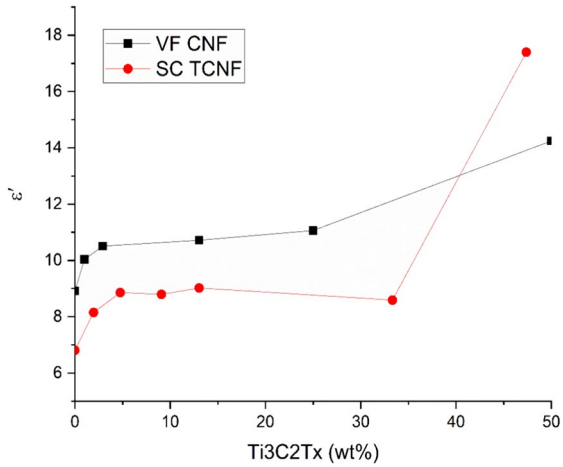

Fig. 8 The evolution of the dielectric permittivity (ε') of VF CNF and SC TCNF-based composite films as a function of $Ti_3C_2T_x$ MXene content, detected at room temperature at the highest (1 MHz) measurement frequency

To compare the influence of $Ti_3C_2T_x$ MXene on the dielectric properties of differently prepared films, first the temperature-dependent dielectric response was investigated of CNF/TCNF-based films prepared

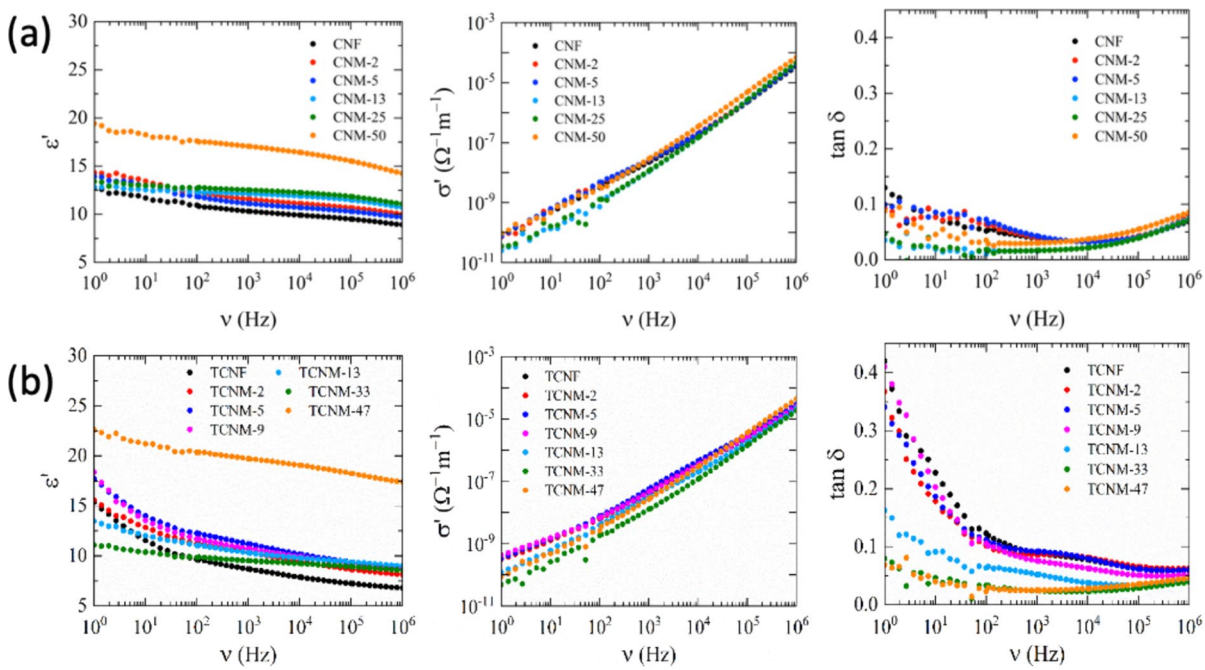

Fig. 7 Frequency dependences of dielectric permittivity (ε'), AC electrical conductivity (ε') and dielectric loss (tan δ), detected at room temperature, for **a** VF CNF and **b** SC TCNF-based films, prepared with and without different contents of (wt%) $Ti_3C_2T_x$ MXene

with 5 wt% of $Ti_3C_2T_x$ addition by both methods (VF and SC) (Fig. 6). It should be stressed once again that, before the measurements, the samples were dried at 100 °C, and then the dielectric response was detected at several frequencies during the cooling runs. While the intrinsic data at the highest frequencies were almost identical for all three samples, the increase in both the low-frequency dielectric constant and electrical conductivity at higher temperatures was much more pronounced for the SC TCNF-based film (TCNM-5). This again suggests that the TCNF-based sample contained a higher amount of free space charges due to the presence of polar – COOH groups. As these charges increase losses and imply the dielectric breakdown at lower electric fields, CNF-based composites seem more suitable for electrical applications. Again, as in the case of pristine films, the preparation method did not affect the free space charges in CNF-based films.

The room-temperature dielectric response of VF CNF-based and SC TCNF-based composite films, prepared with different amounts of $Ti_3C_2T_x$ are presented in Fig. 7. It can be seen that all quantities (ε', σ', and tan δ) increased with increasing the MXene content. Since the dielectric response at lower frequencies is usually governed by extrinsic factors including moisture, the presence of ultra-small dust, free space charges or other impurities contributions, and the presence of Schottky barriers (Pottathara et al. 2016, 2018), the intrinsic material properties were provided at higher measurement frequencies. Figure 8 therefore shows the evolution of the dielectric permittivity, detected at 1 MHz, for VF CNF and SC TCNF-based films as a function of the $Ti_3C_2T_x$ content. The dielectric permittivity of nanocomposites is the measure of the microcapacitors that are formed by the nanofiller, acting as electrodes surrounded with insulating matrices, and the polarization centers that are initiated from the defects and terminated groups on the nanofiller structure (Tu et al. 2018). The enhancement of the dielectric permittivity in the composites, similar to the case where graphene oxide was used as a filler, originates from the synergetic Maxwell–Wagner–Sillars (MWS) polarization effect (Pottathara et al. 2016, 2021) that occurs on the interface between both components. When a current flows through MXene nanosheets and a cellulose matrix, charges accumulate at the interface because of the presence of functional groups (such as – OH and – COOH on CNF/TCNF, and – OH, – O, and – F on MXene), which forms an effective capacitor network. The enhancement in the dielectric permittivity from ~ 8.9 to ~ 14.2 for the CNF-based and from ~ 6.3 to ~ 17.3 for the TCNF-based composites by adding 50 wt% and 47 wt% $Ti_3C_2T_x$, respectively, can be credited to an MWS effect, due to the entrapment of a large number of charge carriers at the interface. Additionally, the interfacial hydrogen bonding between the $Ti_3C_2T_x$ and CNTCNF (already confirmed by FTIR and EDX spectroscopy, Figs. 2 and S4) may also contribute by forming dipoles, and thus increasing the dielectric permittivity.

The electrical conductivity of the composite films (Fig. 7) thus increased from ~ 10^{-11} to ~ 10^{-4} S/m for the CNF-based samples, and from ~ 10^{-10} to ~ 10^{-5} S/m for the TCNF-based composites, with an increase in frequency over the whole investigated frequency range, as well as increased content of $Ti_3C_2T_x$. While at lower frequencies the conductivity of the MXene sheets is effectively blocked, at sufficiently high frequencies their higher conductivity is revealed since most of the charge carriers have no time to feel the blocking boundaries. The intrinsic dielectric loss thus remained below 0.1 for all the developed composites.

Conclusions

The low dielectric permittivity and thermal conductivity of hygroscopic nanocellulose-based materials limit their applications in electronics. In this work, native (CNF) and TEMPO-oxidized (TCNF) cellulose nanofibrils, containing different weight percentages of highly thermally conductive multi-layered $Ti_3C_2T_x$ MXene, were thus prepared, to evaluate the presence of different types of CNFs on the films morphological structure, and, consequently, their moisture absorption ability, dielectric spectroscopic and thermal conductive properties. The dielectric permittivity, dielectric loss and AC conductivity were thus evaluated at different frequencies (1 Hz–1 MHz) and temperatures (273–375 K). In addition, the temperature-dependent thermal diffusivity and conductivity were assessed, to evaluate the effect of air-absorbed moisture on their heat dissipation capacity.

The electrostatic repulsion and hydrogen bonding interaction between the hydrophilic surface/terminal groups on CNF/TCNF and MXene were shown to render their self-assembly distribution and organization into morphologically differently structured films (i.e.more open/porous with randomly distributed CNFs, and densely packed with parallelly aligned TCNFs), and, consequently, different properties. The complementary contribution of the MXene nanosheet structure and moisture absorption ability (32/36%, g/g) of CNF/TCNF to the through-plane thermal conductivity (0.7–1.5/2.8–6.9 W/mK) of composite films prepared with low (up to 5wt%) MXene content was confirmed, which was increasing with the temperature due to the gradual, but kinetically different, release of interphase-absorbed moisture. On the other hand, the lower density and moisture content (20/18%, g/g) of the as-prepared films with higher (50/47wt%) MXene addition, demonstrated relatively low through-plane (0.2–0.5/0.3–0.7 W/mK) but high in-plane (2.5–7.1/6.3–14.4 W/mK) thermal conductivity. The latter was more significant for the TCNF film, whose morphological structure directed the heat transfer between the fibrils and along the nanosheets of integrated multi-layered MXene, indicating its good heat dissipation performance. The as-prepared composite films exhibited relatively high dielectric permittivity (6.3–18) with dielectric losses below 0.1, which shows their potential application in flexible electronic devices.

Acknowledgments The authors are grateful to Vera Vivod, MSc., for performing the moisture absorption testing, and to Prof. Dr. Romana Cerc Korošec for conducting specific heat capacity measurements and helping to interpret the results.

Author contributions Conceptualization, S.L., V.B. and V.K.; Methodology, S.L., V.K. and V.B.; Formal analysis, S.L. and V.J.; Data processing, S.L. and V.J; Writing—original draft preparation, S.L. and V.K.; writing—review and Editing, V.B. and V.K.; Visualization, S.L. and V.K..; Supervision, V.B. and V.K.; Funding acquisition, V.B. and V.K. All the authors have read and approved the final version of the manuscript.

Funding This work was supported by the Slovenian Research and Innovation Agency (Project no. J2-3053 and Programs no. P2-0424 and P1-0125).

Data availability Data are provided within supplementary file.

Declarations

Competing interest The authors declare no competing interests.

Ethical approval This declaration is not applicable.

References

Abdel-karim AM, Salama AH, Hassan ML (2018) Electrical conductivity and dielectric properties of nanofibrillated cellulose thin films from bagasse. J Phys Org Chem 31(9):e3851-3860. https://doi.org/10.1002/poc.3851

Alhabeb M, Maleski K, Anasori B, Lelyukh P, Clark L, Sin S, Gogotsi Y (2017) Guidelines for synthesis and processing of two-dimensional titanium carbide ($Ti_3C_2T_x$ MXene). Chem Mater 29(18):7633–7644. https://doi.org/10.1021/acs.chemmater.7b02847

Anju VP, Narayanankutty SK (2016) Polyaniline coated cellulose fiber / polyvinyl alcohol composites with high dielectric permittivity and low percolation threshold. AIP Adv 6(1):015109. https://doi.org/10.1063/1.4940664

Cao WT, Chen FF, Zhu YJ, Zhang YG, Jiang YY, Ma MG, Chen F (2018) Binary strengthening and toughening of MXene/Cellulose nanofiber composite paper with nacre-inspired structure and superior electromagnetic interference shielding properties. ACS Nano 12(5):4583–4593. https://doi.org/10.1021/acsnano.8b00997

Chen M, Coasne B, Guyer R, Derome D, Carmeliet J (2018a) Role of hydrogen bonding in hysteresis observed in sorption-induced swelling of soft nanoporous polymers. Nat Commun 9:3507. https://doi.org/10.1038/s41467-018-05897-9

Chen YP, Hou X, Kang RY, Liang Y, Guo LC, Dai W, Nishimura K, Lin CT, Jiang N, Yu J (2018b) Highly flexible biodegradable cellulose nanofiber/graphene heat-spreader films with improved mechanical properties and enhanced thermal conductivity. J Mater Chem C 6:12739–12745. https://doi.org/10.1039/C8TC04859B

Chen L, Shi X, Yu N, Zhang X, Du X, Lin J (2018c) Measurement and analysis of thermal conductivity of $Ti_3C_2T_x$ MXene films. Mater 11(9):1701. https://doi.org/10.3390/ma11091701

Chen X, Zhao Y, Li L, Wang Y, Wang J, Xiong J, Du S, Zhang P, Shi X, Yu J (2021) MXene/polymer nanocomposites: preparation, properties, and applications. Polym Rev 61(1):80–115. https://doi.org/10.1080/15583724.2020.1729179

Du G, Wang J, Liu Y, Yuan J, Liu T, Cai C, Luo B, Zhu S, Wei Z, Wang S, Nie S (2023) Fabrication of advanced cellulosic triboelectric materials via dielectric modulation. Adv Sci 10(15):2206243. https://doi.org/10.1002/advs.202206243

Feng Y, Deng Q, Peng C, Wu Q (2019) High dielectric and breakdown properties achieved in ternary $BaTiO_3$ / MXene/PVDF nanocomposites with low-concentration fillers from enhanced interface polarization. Ceram Int 45(6):7923–7930. https://doi.org/10.1016/j.ceramint.2019.01.104

Gao Q, Pan Y, Zheng G, Liu C, Shen C, Liu X (2021) Flexible multilayered MXene/thermoplastic polyurethane films with excellent electromagnetic interference shielding, thermal conductivity, and management performances. Adv Compos Hybrid Mater 4:274–285. https://doi.org/10.1007/s42114-021-00221-4

González J, Ghaffarinejad A, Ivanov M, Ferreira P, Vilarinho PM, Borrás A, Amorín H, Wicklein B (2023) Advanced cellulose–nanocarbon composite films for high-performance triboelectric and piezoelectric nanogenerators. Nanomater 13(7):1206. https://doi.org/10.3390/nano13071206

Habib T, Zhao X, Shah SA, Chen Y, Sun W, An H, Lutkenhaus JL, Radovic M, Green MJ (2019) Oxidation stability of $Ti_3C_2T_x$ MXene nanosheets in solvents and composite films. NPJ 2D Mater Appl 3(1):8

Hu J, Xia H, Hou X, Yang T, Si K, Wang Y, Wang L, Shi Z (2021) Enhanced thermal management performance of nanofibrillated cellulose composite with high thermally conductive boron phosphide. J Mat Chem A 47(9):27049. https://doi.org/10.1039/D1TA06597A

Inui T, Koga H, Nogi M, Komoda N, Suganuma K (2014) High-dielectric paper composite consisting of cellulose nanofiber and silver nanowire. In: 4th IEEE International Conference on Nanotechnology, Toronto, ON, Canada, pp. 470–473. https://doi.org/10.1109/NANO.2014.6967965

Izakura S, Koga H, Uetani, (2021) Humidity-responsive thermal conduction properties of bacterial cellulose films. Cellulose 28:5363–5372. https://doi.org/10.1007/s10570-021-03888-6

Ji S, Jang J, Cho E, Kim SH, Kang ES, Kim J, Kim HK, Kong H, Kim SK, Kim JY, Park JU (2017) High dielectric performances of flexible and transparent cellulose hybrid films controlled by multidimensional metal nanostructures. Adv Mater 29(24):1700538. https://doi.org/10.1002/adma.201700538

Jin XX, Wang JF, Dai LZ, Liu XY, Li L, Yang YY, Cao YX, Wang WJ, Wu H, Guo SY (2020) Flame-retardant poly(vinyl alcohol)/MXene multilayered films with outstanding electromagnetic interference shielding and thermal conductive performances. Chem Eng J 380:122475. https://doi.org/10.1016/j.cej.2019.122475

Jin X, Wang S, Sang C, Yue Y, Xu X, Mei C, Xiao H, Lou Z, Han J (2022) Patternable nanocellulose/$Ti_3C_2T_x$ flexible films with tunable photoresponsive and electromagnetic interference shielding performances. ACS Appl Mater Inter 14(30):35040–35052. https://doi.org/10.1021/acsami.2c11567

Jose J, Thomas V, John J, Mathew RM, Salam JA, Jose G, Abraham R (2021) Effect of temperature and frequency on the dielectric properties of cellulose nanofibers from cotton. J Mater Sci Mater El 32(16):21213–21224. https://doi.org/10.1007/s10854-021-06624-9

Kang R, Zhang Z, Guo L, Cui J, Chen Y, Hou X, Wang B, Lin CT, Jiang N, Yu J (2019) Enhanced thermal conductivity of epoxy composites filled with 2D transition metal carbides (MXenes) with ultralow loading. Sci Rep 9:9135. https://doi.org/10.1038/s41598-019-45664-4

Kovalov KM, Alekseev OM, Lazarenko MM, Zabashta YF, Grabovskii YE, Tkachov SY (2017) Influence of water on the structure and dielectric properties of the microcrystalline and nano-cellulose. Nanoscale Res Lett 12:468. https://doi.org/10.1186/s11671-017-2231-5

Kulasinski K (2017) Free energy landscape of cellulose as a driving factor in the mobility of adsorbed water. Langmuir 33(22):5362–5370. https://doi.org/10.1021/acs.langmuir.7b00914

Le Bras D, Strømme M, Mihranyan A (2015) Characterization of dielectric properties of nanocellulose from wood and algae for electrical insulator applications. J Phys Chem B 119(18):5911–5917. https://doi.org/10.1021/acs.jpcb.5b00715

Li L, Ma Z, Xu P, Zhau B, Li Q, Ma J, He C, Feng Y, Liu C (2020) Flexible and alternant-layered cellulose nanofiber/graphene film with superior thermal conductivity and efficient electromagnetic interference shielding. Compos Part a Appl Sci Manuf 139:106134

Liu R, Li W (2018) High-thermal-stability and high-thermal-conductivity Ti_3C_2Tx MXene/Poly(vinyl alcohol) (PVA) composites. ACS Omega 3:2609–2617. https://doi.org/10.1021/acsomega.7b02001

Liu D, Gao Y, Song Y, Zhu H, Zhang L, Xie Y, Shi H, Shi Z, Yang Q, Xiong C (2022) Highly sensitive multifunctional electronic skin based on nanocellulose/mxene composite films with good electromagnetic shielding biocompatible antibacterial properties. Biomacromol 23(1):182–195. https://doi.org/10.1021/acs.biomac.1c01203

Lunkenheimer P, Bobnar V, Pronin AV, Ritus AI, Volkov AA, Loidl A (2002) Origin of apparent colossal dielectric constants. Phys Rev B 66(5):052105. https://doi.org/10.1103/PhysRevB.66.052105

Luo Q, Shen H, Zhou G, Xu X (2023) A mini-review on the dielectric properties of cellulose and nanocellulose-based materials as electronic components. Carbohyd Polym 303:120449. https://doi.org/10.1016/j.carbpol.2022.120449

Luo Q, Liu Y, Zhou G, Xu X (2024) A new strategy to improve the dielectric properties of cellulose nanocrystals (CNCs): surface modification of small molecules. Carbohyd Polym 324:121451. https://doi.org/10.1016/j.carbpol.2023.121451

Mathis TS, Maleski K, Goad A, Sarycheva A, Anayee M, Foucher AC, Hantanasirisakul K, Shuck CE, Stach EA, Gogotsi Y (2021) Modified MAX Phase synthesis for environmentally stable and highly conductive

Ti_3C_2MXene. ACS Nano 15(4):6420–6429. https://doi.org/10.1021/acsnano.0c08357

Näslund LA, Persson POA, Rosen J (2020) X-ray photoelectron spectroscopy of Ti_3AlC_2, $T_i3_C2_T$z and TiC provides evidence for the electrostatic interaction between laminated layers in MAX-phase materials. J Phys Chem C 124(50):27732–27742. https://doi.org/10.1021/acs.jpcc.0c07413

Pottathara YB, Bobnar V, Gorgieva S, Grohens Y, Finšgar M, Thomas S, Kokol V (2016) Mechanically strong, flexible and thermally stable graphene oxide/nanocellulosic films with enhanced dielectric properties. RSC Adv 6(54):49138–49149. https://doi.org/10.1039/C6RA06744A

Pottathara YB, Bobnar V, Finšgar M, Grohens Y, Thomas S, Kokol V (2018) Cellulose nanofibrils-reduced graphene oxide xerogels and cryogels for dielectric and electrochemical storage applications. Polymer 147:260–270. https://doi.org/10.1016/j.polymer.2018.06.005

Pottathara YB, Bobnar V, Grohens Y, Thomas S, Kargl R, Kokol V (2021) High dielectric thin films based on UV-reduced graphene oxide and TEMPO-oxidized cellulose nanofibers. Cellulose 28(5):3069–3080. https://doi.org/10.1007/s10570-021-03701-4

Shao J, Wang JW, Liu DN, Wei L, Wu SQ, Ren H (2019) A novel high permittivity percolative composite with modified MXene. Polymer 174:86–95. https://doi.org/10.1016/j.polymer.2019.04.057

Song G, Kang R, Guo L, Ali Z, Chen X, Zhang Z, Yan C, Lin CT, Jiang N, Yu J (2020) Highly flexible few-layer Ti_3C_2 MXene/cellulose nanofiber heat-spreader films with enhanced thermal conductivity. New J Chem 44(17):7186–7193. https://doi.org/10.1039/D0NJ00672F

Syamsai R, Kollu P, Jeong SK, Grace AN (2017) Synthesis and properties of 2D-Titanium carbide MXene sheets towards electrochemical energy storage applications. Ceram Int 43(16):13119–13126. https://doi.org/10.1016/j.ceramint.2017.07.003

Tao J, Cao S (2020) Flexible high dielectric thin films based on cellulose nanofibrils and acid oxidized multi-walled carbon nanotubes. RSC Adv 10(18):10799–10805. https://doi.org/10.1039/C9RA10915C

Tao J, Cao S, Liu W, Deng Y (2019) Facile preparation of high dielectric flexible films based on titanium dioxide and cellulose nanofibrils. Cellulose 26(10):6087–6098. https://doi.org/10.1007/s10570-019-02495-w

Tao J, Cao SA, Feng R, Deng Y (2020) High dielectric thin films based on barium titanate and cellulose nanofibrils. RSC Adv 10(10):5758–5765. https://doi.org/10.1039/C9RA10916A

Tao J, Jiao L, Deng Y (2021) Cellulose- and nanocellulose-based dielectric materials. In S. Thomas & Y. B. Pottathara (Eds.), Nanocellulose based composites for electronics, Elsevier Inc ,pp. 73–100. https://doi.org/10.1016/B978-0-12-822350-5.00004-7

Tu SB, Jiang Q, Zhang XX, Alshareef HN (2018) Large dielectric constant enhancement in MXene percolative polymer composites. ACS Nano 12:3369–3377. https://doi.org/10.1021/acsnano.7b08895

Uetani K, Hatori K (2017) Thermal conductivity analysis and applications of nanocellulose materials. Sci Technol Adv Mat 18(1):877–892. https://doi.org/10.1080/14686996.2017.1390692

Uetani K, Kasuya K, Yoshikawa S, Uto T (2022) Tunability of the thermal diffusivity of cellulose nanofibril films by addition of multivalent metal ions. Carbohyd Polym 297:120010. https://doi.org/10.1016/j.carbpol.2022.120010

Wang C, Hua L, Yan H, Li B, Tu Y (2020) A thermal management strategy for electronic devices based on moisture sorption-desorption processes. Joule 4(2):435–447. https://doi.org/10.1016/j.joule.2019.12.005

Wang Z, Lee YH, Kim SW, Seo JY, Lee SY, Nyholm L (2021) Why cellulose-based electrochemical energy storage devices? Adv Mater 33(28):2000892. https://doi.org/10.1002/adma.202000892

Wang G, Kudo M, Daicho K, Harish S (2022a) Enhanced high thermal conductivity cellulose filaments via hydrodynamic focusing. Nano Lett 22(21):8406–8412. https://doi.org/10.1021/acs.nanolett.2c02057

Wang HQ, Wang JW, Wang XZ, Gao XH, Zhuang GC, Yang JB, Ren H (2022b) Dielectric properties and energy storage performance of PVDF-based composites with MoS2@MXene nanofiller. Chem Eng J 437(2):135431. https://doi.org/10.1016/j.cej.2022.135431

Wang P, Yin Y, Fang L, He J, Wang Y, Cai H, Yang Q, Shi Z, Xiong C (2023) Flexible cellulose/PVDF composite films with improved breakdown strength and energy density for dielectric capacitors. Compos Part A 164:107325. https://doi.org/10.1016/j.compositesa.2022.107325

Windmill JFC, Zorab A, Bedwell DJ, Robert D (2007) Nanomechanical and electrical characterization of a new cellular electret sensor–actuator. Nanotechnology 19(3):035506. https://doi.org/10.1088/0957-4484/19/03/035506

Xu Y, Chen X, Zhang C, Ragauskas AJ, Wen JL, Zhao P, Si C, Xu T, Song X (2022) Enhancing thermal conductivity and toughness of cellulose nanofibril/boron nitride nanosheet composites. Carbohyd Polym 296:119938. https://doi.org/10.1016/j.carbpol.2022.119938

Yan YZ, Li S, Park SS, Zhang WJ, Lee JS, Kim JR, Seong DG, Ha CS (2023) One stone, two birds solvent system to fabricate microcrystalline cellulose-$Ti_3C_2T_x$ nanocomposite film as a flexible dielectric and thermally conductive material. Nano Res 16:3240–3253. https://doi.org/10.1007/s12274-022-5062-3

Yang W, Kim J (2022) Enhancing the through-plane thermal conductivity of a cellulose nanofiber film via boron nitride surface functionalization and cellulose chemical crosslinking. Ceram Inter 48(17):25284–25291. https://doi.org/10.1016/j.ceramint.2022.05.193

Yang JB, Wang JW, Zhuang GC, Wang XZ, Wang HQ, Ma YJ, Zhang Y (2023) High dielectric constant acrylic resin based percolative composite with acidified carbon nanotubes intercalation of MXene. Eur Polym J 190:112006. https://doi.org/10.1016/j.eurpolymj.2023.112006

Yu L, Huang D, Wang X, Yu W (2022) Yue Y (2022) Tuning thermal and electrical properties of MXenes via dehydration. Phys Chem Chem Phys 24:25969. https://doi.org/10.1039/D2CP03619C

Yun GY, Kim JH, Kim J (2009) Dielectric and polarization behaviour of cellulose electroactive paper (EAPap). J Phys D: Appl Phys 42(8):082003. https://doi.org/10.1088/0022-3727/42/8/082003

Zeng X, Deng L, Yao Y, Sun R, Xu J, Wong CP (2016) Flexible dielectric papers based on biodegradable cellulose nanofibers and carbon nanotubes for dielectric energy storage. J Mater Chem C 4(25):6037–6044. https://doi.org/10.1039/C6TC01501H

Zeng XL, Sun JJ, Yao YM, Sun R, Xu JB, Wong CP (2017) A combination of boron nitride nanotubes and cellulose nanofibers for the preparation of a nanocomposite with high thermal conductivity. ACS Nano 11(5):5167–5178. https://doi.org/10.1021/acsnano.7b02359

Zeng Y, Xiong C, Li W, Rao S, Du G, Fan Z, Chen N (2022) Significantly improved dielectric and mechanical performance of $Ti_3C_2T_x$ MXene/silicone rubber nanocomposites. J Alloy Compd 905:164172. https://doi.org/10.1016/j.jallcom.2022.164172

Zeng Y, Tang L, Xin Z, Guo F, Li G, Chen N, Du G (2023) Ti_3C_2Tx MXene-Ag/silicone rubber composites with enhanced dielectric properties and improved mechanical properties. J Alloy Compd 930:167419. https://doi.org/10.1016/j.jallcom.2022.167419

Zhan Z, Song Q, Zhou Z, Lu C (2019) Ultrastrong and conductive MXene/cellulose nanofiber films enhanced by hierarchical nano-architecture and interfacial interaction for flexible electromagnetic interference shielding. J Mater Chem C 7(32):9820–9829. https://doi.org/10.1039/C9TC03309B

Zhang T, Pan L, Tang H (2017) Synthesis of two-dimensional Ti_3C_2Tx MXene using HCl+LiF etchant: Enhanced exfoliation and delamination. J Alloy Compd 695:818–826. https://doi.org/10.1016/j.jallcom.2016.10.127

Zhao Y, Jiang C, Xiong Y, Ma Y, Zhang T, Zhang X, Qin J, Shi X, Zhang G (2023) Flexible and robust TEMPO-oxidized cellulose nanofibrils/mica composite as paper dielectrics with enhanced dielectric property. J Mater Sci Mater El 34(4):330. https://doi.org/10.1007/s10854-022-09761-x